

Supporting Information for "Coupling two distant double quantum dots to a microwave resonator"

Guang-Wei Deng^{†,1,2} Da Wei^{†,1,2} Shu-Xiao Li^{1,2} J.R. Johansson,³ Wei-Cheng Kong,^{1,2} Hai-Ou Li,^{1,2} Gang Cao,^{1,2} Ming Xiao,^{1,2} Guang-Can Guo,^{1,2} Franco Nori,^{4,5} Hong-Wen Jiang,⁶ and Guo-Ping Guo^{1,2,*}

¹Key Laboratory of Quantum Information, University of Science and Technology of China, Chinese Academy of Sciences, Hefei 230026, China

²Synergetic Innovation Center of Quantum Information & Quantum Physics, University of Science and Technology of China, Hefei, Anhui 230026, China[†]

³iTHES research group, RIKEN, Wako-shi, Saitama, 351-0198 Japan

⁴CEMS, RIKEN, Wako-shi, Saitama, 351-0198 Japan

⁵Physics Department, The University of Michigan, Ann Arbor, Michigan 48109-1040, USA

⁶Department of Physics and Astronomy, University of California at Los Angeles, California 90095, USA

I. SAMPLE FABRICATION AND MEASUREMENT SETUP

The samples are fabricated as follows. First we mechanically exfoliated the graphene from its bulk, KISH graphite (Kyocera. Inc), to an undoped silicon chip with 285 nm oxide. In this experiment we need two pieces of few-layer graphene with proper distance between 20 to 80 μm , and we selected those that met this requirement. Second, electron beam lithography (EBL) was employed several times, starting with the fabrication of alignment marks, then plasma-etching masks and electrode patterns. The EBL resists used were PMMA 950k A4 for the first step and double-layered PMMA 950k A2 for the latter two steps. We developed the sub-micrometer patterns under 0 °C to establish a better control of the device specifications. Through etching out all the undesired part of the graphene sheet to realize the designed device, we strove for the all-metal-side-gated configuration as described in Ref. [1], to avoid unstable gate terminals. This etching was carried out by inductively-coupled plasma (ICP), using a 4:1 gas mixture of Oxygen to Argon. For marks and electrodes we deposited 5 nm Ti and 45 nm Au with an electron-beam evaporator. Finally, the resonator was fabricated by optical lithography followed by metal deposition in a thermal evaporator. The metal used was 200-nm-thick Al.

The microwave response was measured using a network analyzer (NA). The input and output ports of the NA were connected to the resonator via a circulator and a 180 degree hybrid, which splits the reflected signal back to the NA. Two 30 dB attenuators were connected between the NA output port and the circulator, reducing the power applied to the resonator down to lower than -130 dBm. The reflected signal was amplified first at 4 K and then at room temperature, producing an additional gain of 60 dB, and an isolator was used to prevent noise from the amplifiers and the environment from reaching the sample. The direct transport current was amplified by a low-noise

current pre-amplifier, before being measured by a digital multimeter.

II. MEASUREMENT OF TWO DQDS

First, we measure the lever arm α of each gate. From the constant interaction model [2], we know that when tuning the gate voltage along the red dashed line in Fig. S1(b) (i.e., $k_{AC} = -\frac{C_{gL}}{C_{gR}} \cdot \frac{C_R}{C_M}$), the electrochemical potential of the left dot μ_L remains unchanged while that of the right dot μ_R shifts. Therefore, we may study the charging effect of the right dot, with its gate-controlled energy written as

$$\begin{aligned} \Delta\mu_R(\Delta V_{gL}, \Delta V_{gR}) &= -\frac{1}{|e|} (C_{gL} E_{CM} \Delta V_{gL} + \\ &C_{gR} E_{CR} k_{AC} \Delta V_{gL}) \\ &= |e| \frac{C_{gL}}{C_M} \Delta V_{gL} \\ &= |e| \alpha_{LM} \Delta V_{gL}, \end{aligned} \quad (1)$$

where $E_{CL} = \frac{C_R}{C_L C_R - C_M^2}$, $E_{CR} = \frac{C_L}{C_L C_R - C_M^2}$, and $E_{CM} = \frac{C_M}{C_L C_R - C_M^2}$.

Additionally, by sweeping the bias voltage V_{SD} , a Coulomb diamond appears, giving $|e|V_{SD} = |e|\alpha_{LM}\Delta V_{gL}$ (Fig. S1b). Then we have

$$\alpha_{LM} = \frac{V_{SD}}{\Delta V_{gL}} = \left(\frac{1}{k^+} + \frac{1}{|k^-|} \right)^{-1}. \quad (2)$$

Similarly, along the green line in Fig. S1(b) (i.e., $k_{AD} = -\frac{C_{gL}}{C_{gR}} \cdot \frac{C_M}{C_L}$), we obtain

$$\Delta\mu_L = |e| \frac{C_{gR}}{C_M} \Delta V_{gR} = |e| \alpha_{RM} \Delta V_{gR}. \quad (3)$$

Using the expressions for k_{AC} and k_{AD} , we obtain the lever arm of each gate

$$\alpha_L = \frac{C_{gL}}{C_L} = -k_{AD} \alpha_{RM}, \quad (4)$$

* Corresponding author: gpguo@ustc.edu.cn

[†] These authors contributed equally to this work.

$$\alpha_R = \frac{C_{gR}}{C_R} = -\frac{1}{k_{AC}}\alpha_{LM}. \quad (5)$$

Now we derive the relation between gate voltage ΔV_{gL} and energy detuning ϵ during the sweep. The expressions

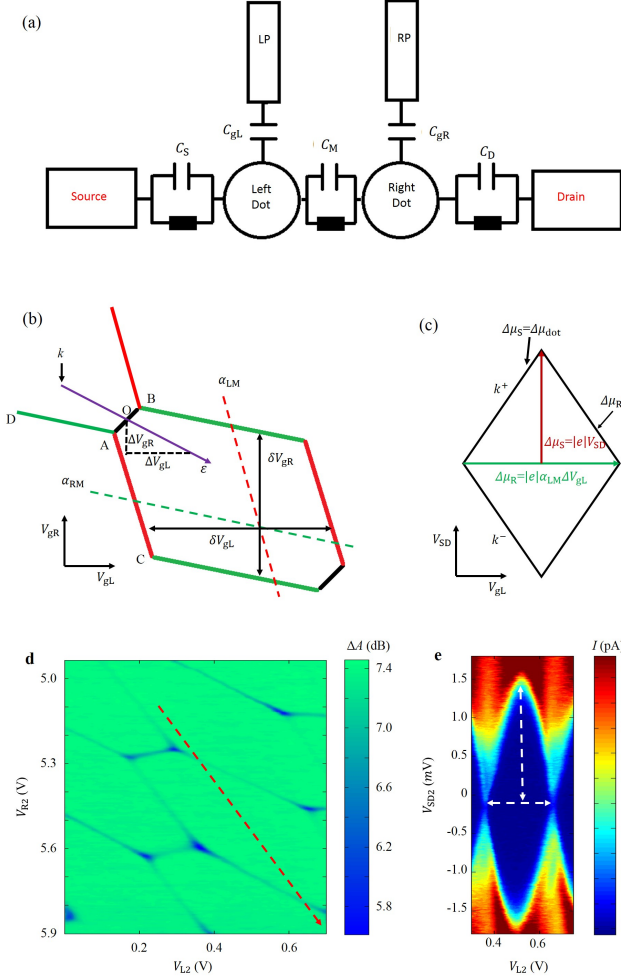


FIG. S1. (a) Schematic diagram of a DQD. (b) Schematic picture of the charge-stability diagram for a DQD using the constant interaction model. The red and green dashed lines are each parallel to an edge of the honeycomb, along which only one dot's energy level changes. Additionally, by applying different bias voltages, we obtain a Coulomb diamond. The purple arrow across AB indicates the sweep direction when treating the DQD as a two-level system. (c) Schematic diagram of Coulomb diamond obtained by sweeping gate voltages along the dashed red line in b. Analyzing the energy shift as a function of the voltages, we can obtain α_{LM} . (d-e) A typical charge-stability diagram (d) and Coulomb diamond (e) of DQD2 in our device. (e) is obtained from the dashed red arrow in (d). From the white arrows in (e), the lever arm α_{LM} can be obtained.

for μ_L and μ_R are

$$\mu_L(N, M; V_{gL}, V_{gR}) = \left(N - \frac{1}{2}\right) E_{CL} + M E_{CM} - \frac{1}{|e|} (C_{gL} V_{gL} E_{CL} + C_{gR} V_{gR} E_{CM}), \quad (6)$$

$$\mu_R(N, M; V_{gL}, V_{gR}) = N E_{CM} + \left(M - \frac{1}{2}\right) E_{CR} - \frac{1}{|e|} (C_{gL} V_{gL} E_{CM} + C_{gR} V_{gR} E_{CR}), \quad (7)$$

taking the difference between them gives

$$\begin{aligned} \epsilon &= \epsilon(\Delta V_{gL}, \Delta V_{gR}) = -\frac{1}{|e|} [C_{gL}(E_{CL} - E_{CM})\Delta V_{gL} - C_{gR}(E_{CR} - E_{CM})\Delta V_{gR}] \\ &= -|e| \left[\frac{\alpha_L + k_{AD}\alpha_R}{1 - \frac{k_{AD}}{k_{AC}}} - \frac{\alpha_R + \frac{1}{k_{AC}}\alpha_L}{1 - \frac{k_{AD}}{k_{AC}}} k \right] \Delta V_{gL}. \end{aligned} \quad (8)$$

Here k is the slope in the gate voltage sweep process (Fig. S1b). Substituting α_L and α_R with parameters in Fig. S1b yields

$$\alpha_L + k_{AD}\alpha_R = \frac{C_{gL}}{C_L} \frac{C_R - C_M}{C_R}, \quad (9)$$

$$\alpha_R + \frac{1}{k_{AC}}\alpha_L = \frac{C_{gR}}{C_R} \frac{C_L - C_M}{C_L}. \quad (10)$$

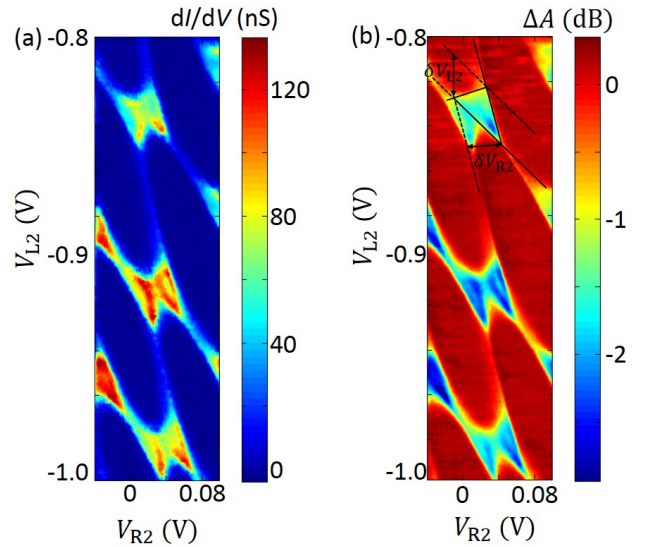


FIG. S2. Typical bias triangle, obtained by transport measurements (left) and the resonator signal (right). The gate lever arms can be obtained by measuring the triangle size.

With $k_{AB} = \frac{C_{gL} C_R - C_M}{C_{gR} C_L - C_M}$ (the slope from point A to B in Fig. S1b), and $C_{gL(R)} = \frac{|e|}{\delta V_{gL(R)}}$, finally we have

$$\epsilon = -|e|\alpha_L \frac{1 - \frac{k}{k_{AB}}}{1 - \frac{k_{AD}}{k_{AB}}} \left(1 + \frac{1}{k_{AC}} \frac{\delta V_{gR}}{\delta V_{gL}} \right) \Delta V_{gR}. \quad (11)$$

III. TAVIS-CUMMINGS MODEL

In the joint-readout experiment, our sample can be seen as two quantum two-level systems that are dipole coupled to a resonator, and it can therefore be described by the Tavis-Cummings Hamiltonian [3]

$$H = \omega_0 a^\dagger a + \sum_{i=1,2} \left[\frac{1}{2} \Omega_i \sigma_{zi} + g_i (\sigma_{+i} a + \sigma_{-i} a^\dagger) \right], \quad (12)$$

where $g_i = g_{Ci} \frac{2t_{Ci}}{\Omega_i}$ and $\Omega_i = \sqrt{(2t_{Ci})^2 + \epsilon_i^2}$. Here ω_0 is the resonant frequency of the resonator, ϵ_i , t_{Ci} and g_{Ci} denote the detuning, the tunneling matrix element and the DQD-resonator coupling constant of DQD i , respectively. To determine the reflected signal, using input-output theory [4], we write down the Heisenberg-Langevin equations of motion for the operators a and σ_{i-}

$$\dot{a}(t) = -j\omega_0 a(t) - j\sum_{i=1,2} g_i \sigma_{i-} - \frac{1}{2}(\kappa_e + \kappa_i) a(t) + \sqrt{\kappa_e} a_{in}(t), \quad (13)$$

$$\dot{\sigma}_{i-}(t) = -j\omega_i \sigma_{i-}(t) + jg_i a(t) \sigma_{zi}(t) - \frac{1}{2}\gamma_{1i} \sigma_{i-}(t) - \gamma_{2i} \sigma_{i-}(t), \quad (14)$$

where κ_e (κ_e) is the external (internal) dissipation rate of the resonator. In what follows, we assume that the quantum dot stays in its ground state, leading to the replacement $\sigma_{zi} \rightarrow -1$. Fourier transformation of the

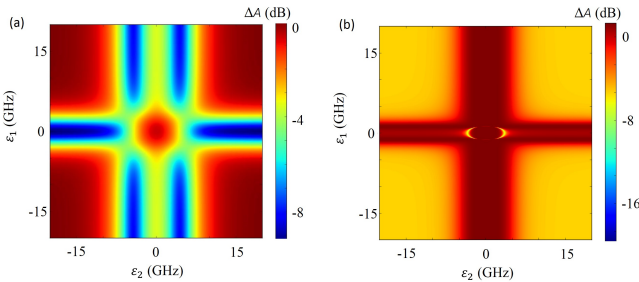


FIG. S3. Amplitude (a) and phase (b) simulation results of the weak-coupling regime, which is similar to our experimental results. The DQD parameters are $g_{C1}=40$ MHz, $g_{C2}=29$ MHz, $2t_{C1}=7.2$ GHz, $2t_{C2}=7.2$ GHz, $\Gamma_1 = (\frac{\gamma_1}{2} + \gamma_2)_{DQD1}=3.6$ GHz, $\Gamma_2 = (\frac{\gamma_1}{2} + \gamma_2)_{DQD2}=3.0$ GHz, where $g_{C1}(g_{C2}) < \Gamma_1(\Gamma_2)$.

remaining linear equations then gives

$$-j\omega \sigma_{i-}(\omega) = -j\Omega_i \sigma_{i-}(\omega) - jg_i a(\omega) - \frac{1}{2}\gamma_{1i} \sigma_{i-}(\omega) - \gamma_{2i} \sigma_{i-}(\omega), \quad (15)$$

$$-j\omega a(\omega) = -j\Omega_0 a(\omega) - j\sum_{i=1,2} g_i \sigma_{i-}(\omega) - \frac{1}{2}(\kappa_e + \kappa_i) a(\omega) + \sqrt{\kappa_e} a_{in}(\omega). \quad (16)$$

Using the boundary condition $a_{in} + a_{out} = \sqrt{\kappa_e} a$, combined with the results above, we obtain

$$\sigma_{i-}(\omega) = -\frac{jg_i}{j(\Omega_i - \omega) + \frac{1}{2}\gamma_{1i} + \gamma_{2i}} a(\omega) = -j\chi_i a(\omega), \quad (17)$$

$$\left[j(\omega_0 - \omega) + g_1 \chi_1 + g_2 \chi_2 + \frac{1}{2}(\kappa_e + \kappa_i) \right] a(\omega) = \sqrt{\kappa_e} a_{in}(\omega). \quad (18)$$

Finally, we obtain the input-output relation

$$S_{11} = \frac{a_{out}}{a_{in}} = -\frac{j(\omega_0 - \omega) + g_1 \chi_1 + g_2 \chi_2 + \frac{1}{2}(\kappa_i - \kappa_e)}{j(\omega_0 - \omega) + g_1 \chi_1 + g_2 \chi_2 + \frac{1}{2}(\kappa_i + \kappa_e)}, \quad (19)$$

$$\chi_i = \frac{g_i}{j(\Omega_i - \omega) + \frac{1}{2}\gamma_{1i} + \gamma_{2i}}, \quad i = 1, 2. \quad (20)$$

To compare this to our experimental data, instead of S_{11} , we define the amplitude $A = 20\log|S_{11}|$ and the argument $\phi = \arg(S_{11})$. Here A is in dB unit and ϕ is in units of degrees. Both of them can be directly measured by a network analyzer. With the parameters of each

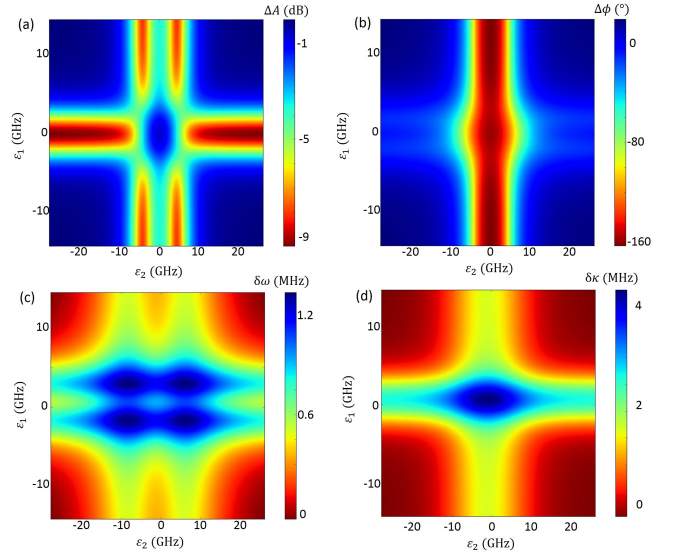


FIG. S4. (a) Frequency shift as a sum of the shift due to each DQD. (b) Internal decay rate increase.

DQD obtained by independent experiments following the method in Ref. [5], we can reproduce the joint-readout results in Fig. 3 in the main text. In this case, the DQD parameters used are $g_{C1}=40$ MHz, $g_{C2}=29$ MHz, $2t_{C1}=7.2$ GHz, $2t_{C2}=7.2$ GHz, $\Gamma_1 = (\frac{\gamma_1}{2} + \gamma_2)_{\text{DQD1}}=3.6$ GHz, $\Gamma_2 = (\frac{\gamma_1}{2} + \gamma_2)_{\text{DQD2}}=3.0$ GHz, and the resonator parameters are $\kappa_i/2\pi=0.684$ MHz, $\kappa_i/2\pi=1.318$ MHz, $\omega_0/2\pi=6.35086$ GHz. Figure S4 shows two typical simulation results for amplitude response (a) and phase response (b) of the resonator that are representative for the weak-coupling regime. However, due to the large dephasing rates in DQD systems, we cannot reach the strong-coupling regime in our device.

From equation (19), it is clear that the effect of the two DQDs on the resonator signal S_{11} is the term $g_1\chi_1 + g_2\chi_2$, where χ_i is the susceptibility [6] caused by the i th DQD. If we write $g_1\chi_1 = \delta\kappa_1 + j\delta\omega_1$, $g_2\chi_2 = \delta\kappa_2 + j\delta\omega_2$, and define $\delta\omega = \delta\omega_1 + \delta\omega_2$, $\delta\kappa = \delta\kappa_1 + \delta\kappa_2$, then equation (19) can be rewritten as

$$S_{11} = -\frac{j[(\omega_0 + \delta\omega) - \omega] + \frac{1}{2}[(2\delta\kappa + \kappa_i) - \kappa_e]}{j[(\omega_0 + \delta\omega) - \omega] + \frac{1}{2}[(2\delta\kappa + \kappa_i) + \kappa_e]}, \quad (21)$$

where $\delta\omega$ is the resonator frequency shift due to the DQDs, and $2\delta\kappa$ is the change of the internal resonator decay rate due to the DQDs, which produces a broadening of the linewidth. Notice that $g_i\chi_i = 0$ when $\epsilon_i \rightarrow \infty$, leading to a pure resonator response. Now we define the contribution of the DQDs to the signal using

$$\Delta A(\epsilon_1, \epsilon_2) = A(\epsilon_1, \epsilon_2) - A(\infty, \infty) = \Delta A(\delta\omega; \delta\kappa), \quad (22)$$

$$\Delta\phi(\epsilon_1, \epsilon_2) = \phi(\epsilon_1, \epsilon_2) - A(\infty, \infty) = \Delta\phi(\delta\omega; \delta\kappa). \quad (23)$$

The ϵ_i -induced frequency shift and internal decay increase can be written as $\delta\omega_1 + \delta\omega_2$ and $2\delta\kappa_1 + 2\delta\kappa_2$, respectively (see Fig. S5). However, since S_{11} is non-linear in these variables, ΔA and $\Delta\phi$ are not additive, i.e., $\Delta A \neq \Delta A(\epsilon_1, \infty) + \Delta A(\infty, \epsilon_2)$, $\Delta\phi \neq \Delta\phi(\epsilon_1, \infty) + \Delta\phi(\infty, \epsilon_2)$. This phenomenon is observed in our joint readout experiment, and the results are explained by the T-C model, as shown in the main text (see Fig. 3).

In the T-C model, there is a coherent coupling between the DQDs mediated by the resonator which allows the DQDs to exchange both real or virtual photons with the resonator. This is in contrast to the results in Fig. S3, where ΔA and $\Delta\phi$ sum directly. At the cross point, as the charging energy is much larger than photon energy, the signal indicates a quantum admittance, which is a linear response [7]. This kind of direct summation in ΔA and $\Delta\phi$ leads to a direct-crossing picture [Fig. S3(e,f)]. However, the T-C model show a non-linear relation in the ΔA diagram (Fig. S4a).

There may be higher-order processes in this kind of hybrid system, especially when two DQDs are source-drain biased, and these processes could contribute to the current and low-frequency noise in both DQDs [8–10]. In our joint readout measurements (see Fig. 3), all leads were grounded in order to avoid higher-order processes, as such effects are not included in the T-C Hamiltonian.

IV. TUNABILITY OF THE ENERGY LEVEL-SPLITTINGS IN SQD AND DQD DEVICES

In this section we analyze and compare the tunability of the energy-level splittings in SQD and DQD devices. In QD devices, there are two types of discrete energy levels, the charging energy and the single particle energy levels. The former stems from the physics of charged particles confined in a box, interacting through the Coulomb interaction. The level spacing, usually referred to as ‘‘charging energy’’, denoted as E_C , is the energy needed to add one more electron into the QD and its value primarily depends on the size of the QD. Typical values of E_C range from 1 to 100 meV [2, 11], which is far larger than the energy scale of the resonator photons (~ 30 μeV). Single particle energy levels are due to internal degrees of freedom, such as orbit and spin. For spin degrees of freedom, inducing and controlling the energy-level splitting requires application of an external magnetic field. Note that Al ceases to be superconducting when the external field exceeds 300 mT, and this sets an upper limit on the obtainable Zeeman splitting of the spin states. In addition, applying a magnetic field not only changes the desired energy splitting, it would likely also change other properties of the sample dramatically. For orbital degrees of freedom (also often be referred to as charge states), the energy splitting ranges from ~ 10 μeV to ~ 1 meV. Admittedly, it covers our desired range. However, gate-potential-defined SQD devices are usually implemented with plunger gates and defining gates. Tuning the plunger-gate potential shifts the energy levels in the QD as a whole and leaves the energy-level splitting unchanged. For the defining gates, the changes in the defining potential change both the shape and the size of the QD. Experimentally, it requires great effort to tune the energy splitting without changing other fundamental properties, including the QD shape and the barrier tunneling rates. Regarding the shape-defined SQDs, such as carbon nanotubes and etched graphene nanoribbons, control over the single particle energy level splitting is even more difficult. The DQDs are formed either by their shape or applied potentials. Still, near a transition line in the charge-stability diagram, the energy splitting between the charge states in the left and right dot is $\Omega = \sqrt{\epsilon^2 + (2t_C)^2}$. This splitting can be directly controlled by gate voltages. Note that $2t_C$ typically ranges from 1 to ~ 100 μeV .

V. CALIBRATION OF THE NOISE MEASUREMENT SETUP

The noise measurement in our group were made after two pre-amplifiers (SR570) by a dynamic signal analyzer (SR785), this machine can sensitively measure the noise of a current and cross-noise between two sources. Using this machine in our lab, we have measured the

charge noise of an undoped GaAs DQD [12] and a suspended graphene QD [13]. Here we use this machine to measure the cross-noise. We did the RMS Average in the experiment. The cross-noise we measured was: $S_{12} = FFT^*(I1) \times FFT(I2)$, and we did 10 times RMS average for a better resolution before taking the data out from the SR785. The SR785 do the Fourier transform:

$$S_{12} = FFT^*(I1) \times FFT(I2) = FFT \int I1(t)I2(\tau + t)dt \quad (24)$$

In the experiment, the integral time cannot be really infinite, in Figure 4c we choose the integral time about 4s (very long time when compared to the single acquisition time, the maximum acquisition rate of our machine SR785 is 102.4 KHz). 1/f noise in QD-based circuit QED systems has been reported recently [14]. In that paper, the authors measured the charge noise of a GaAs DQD using the resonator and found a 1/f type noise spectrum which was consistent with previous QPC detectors. Here in this experiment, we measured the 1/f noise of the DQD, by SR785 (See Fig. S5a). Compared to the cross-correlation noise spectrum S_{12} , here we define the uncorrelated noise spectrum density $S_{12}^* = |FFT(I1)| \times |FFT(I2)| = S_1 \times S_2$ (See Fig. S5b), which represents the direct multiplying of the two DQDs' 1/f noise. We find that S_{12}^* and S_{12} are both of the order of $10^{-27} A^2 Hz^{-1}$ at $\epsilon_2 = 0$. Thus we conclude that, the central peak in Fig. S5c (and Fig. 4c in the main text) at $\epsilon_2 = 0$, is possibly correlated to that of the individual device 1/f noises S_1 and S_2 . However, the two side peaks cannot be produced by the detuning dependence of S_{12}^* in Fig. S5b (red arrows in above figure). Therefore, the two anomalous side peaks likely represent the photon mediated processes between the two DQDs (i.e., one DQD emits photon into the resonator and will be absorbed by another

DQD). Indeed, previous theoretical work [10] has predicted such photon-mediated current cross-correlations. Previous theoretical work [10] has also reported that the current cross-correlations are not sensitive to the thermally assisted transport processes and the main contribution to the current cross-correlation comes from S_{12} , not from S_{11} nor S_{22} (S_{11} and S_{22} are auto-correlation noise from DQD1 and DQD2, respectively). In this sense, the 1/f noise from any one of the two DQDs will not affect the F_{12} measurement, and this is why the previous theoretical works [8–10] suggest to measure F_{12} instead of directly measure the conductance. Only the cavity decay rate can reduce the cross-correlations. Bandwidth of our noise setup ranges from 125 mHz to 102.4 kHz, which limits by the dynamic signal analyzer SR785. The F_{12} data shown in the manuscript comes from the smallest frequency, which is called zero-frequency cross-noise. (Frequency cannot be really zero, it is 125 mHz indeed, limited by the machine.)

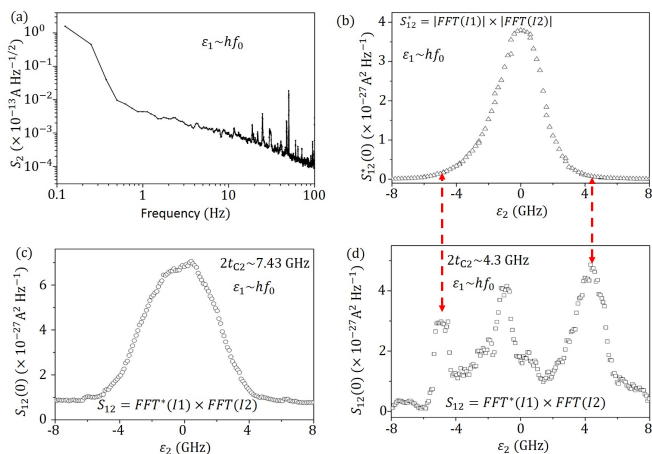


FIG. S5. (a) Current noise of DQD2, measured by SR785. (b) Uncorrelated noise density, obtained by directly multiplying noise spectrum of the two DQDs. (c-d) Cross-spectrum of the two DQDs, measured at different $2t_C$ values.

-
- [1] D. Wei, H.-O. Li, G. Cao, G. Luo, Z.-X. Zheng, T. Tu, M. Xiao, G.-C. Guo, H.-W. Jiang, and G.-P. Guo, *Sci. Rep.* **3**, 3175 (2013).
- [2] W. G. van der Wiel, S. De Franceschi, J. M. Elzerman, T. Fujisawa, S. Tarucha, and L. P. Kouwenhoven, *Rev. Mod. Phys.* **75**, 1 (2002).
- [3] M. Tavis and F. W. Cummings, *Phys. Rev.* **170**, 379 (1968).
- [4] C. W. Gardiner and M. J. Collett, *Phys. Rev. A* **31**, 3761 (1985).
- [5] G.-W. Deng, D. Wei, J. J., R., M.-L. Zhang, S.-X. Li, H.-O. Li, G. Cao, M. Xiao, T. Tu, G.-C. Guo, H.-W. Jiang, N. Franco, and G.-P. Guo, arXiv: 1310.6118 (2013).
- [6] K. D. Petersson, W. McFaul, L., D. Schroer, M., M. Jung, M. Taylor, J., A. Houck, A., and R. Petta, J., *Nature* **490**, 380 (2012).
- [7] T. Frey, J. Leek, P., M. Beck, J. Faist, A. Wallraff, K. Ensslin, T. Ihn, and M. Buttiker, *Phys. Rev. B* **86**, 115303 (2012).
- [8] C. Bergenfeldt and P. Samuelsson, *Phys. Rev. B* **87**, 195427 (2013).
- [9] L. D. Contreras-Pulido, C. Emary, T. Brandes, and R. Aguado, *New J. Phys.* **15**, 095008 (2013).
- [10] N. Lambert, C. Flindt, and F. Nori, *EPL* **103**, 17005 (2013).
- [11] L.-J. Wang, G. Cao, T. Tu, H.-O. L, C. Zhou, X.-J. Hao, Z. Su, G.-C. Guo, H.-W. Jiang, and G.-P. Guo, *Appl. Phys. Lett.* **97**, 262113 (2010).
- [12] H.-O. Li, G. Cao, M. Xiao, J. You, D. Wei, T. Tu, G.-C. Guo, H.-W. Jiang, and G.-P. Guo, *J. Appl. Phys.* **116**, 174504 (2014).
- [13] X.-X. Song, H.-O. Li, J. You, T.-Y. Han, G. Cao, T. Tu, M. Xiao, G.-C. Guo, H.-W. Jiang, and G.-P. Guo, *Sci. Rep.* **5**, 8142 (2015).
- [14] J. Basset, A. Stockklauser, D. D. Jarausch, T. Frey, C. Reichl, W. Wegscheider, K. Ensslin, A. Wallraff, and T. M. Ihn, *Appl. Phys. Lett.* **105**, 063105 (2014).